A kinetic study of the reactions of iron oxides and hydroxides relevant to the chemistry of iron in the upper mesosphere

Daniel E. Self and John M. C. Plane*

School of Environmental Sciences, University of East Anglia, Norwich, UK NR4 7TJ

This paper describes the kinetic study of a number of gas-phase reactions of iron oxides and hydroxides with O, H and O_3. These reactions are important for characterising the chemistry of meteor-ablated iron in the earth's upper mesosphere. Pulses of atomic Fe were produced in the upstream section of a fast flow tube by the pulsed laser ablation of a pure Fe rod, and detected at the downstream end by LIF at 248.3 nm $Fe(x^5F^0_5 \leftarrow a^5D_4)$. The Fe-containing reactant species FeO and FeO_2 were produced by sequential reaction of Fe with NO_2; FeO_3 by the reaction of metastable excited Fe atoms with O_2 to form FeO, followed by addition of O_2; and $Fe(OH)_2$ by the addition of H_2O to FeO. Atomic O or H was produced by the microwave discharge of N_2 (with addition of NO) or H_2, respectively, and their absolute concentrations determined by conventional titration with NO_2. Rate coefficients were essentially measured *relative* to absolute rate coefficients for Fe and FeO determined previously [J. M. C. Plane and R. J. Rollason, *Phys. Chem. Chem. Phys*, 1999, **1**, 1843; R. J. Rollason and J. M. C. Plane, *ibid.*, 2000, **2**, 2335], but were extracted using a full kinetic model including diffusive loss on the flow tube walls of the relevant species. The following results were obtained (units: cm^3 molecule^{-1} s^{-1}; quoted uncertainty is 2σ): $k(FeO + O \rightarrow Fe + O_2$, 209–381 K$) = 4.6^{+2.6}_{-1.6} \times 10^{-10}$ e$^{-(350\pm130)/T}$; $k(FeO_2 + O \rightarrow FeO + O_2$, 209–381 K$) = 1.4^{+0.8}_{-0.5} \times 10^{-10}$ e$^{-(580\pm120)/T}$; $k(FeO_3 + O \rightarrow FeO_2 + O_2$, 610 K$) = 8^{+10}_{-5} \times 10^{-12}$; $k(FeO_2 + O_3 \rightarrow FeO_3 + O_2$, 224–298 K$) = 4.4^{+6.4}_{-2.6} \times 10^{-10}$ e$^{-(170\pm230)/T}$; $k(FeO_3 + H \rightarrow FeOH + O_2$, 294 K$) = (2.0^{+1.2}_{-0.6}) \times 10^{-11}$, and $k(FeOH + H \rightarrow$ products, 294 K$) = (1.3 \pm 0.3) \times 10^{-11}$. Theoretical calculations at the B3LYP/6-311 + g(2d,p) level were used to identify the stationary points on the relevant potential energy surfaces for most of these reactions, before applying statistical theories to model the kinetics. The implications of these results for the chemistry of iron in flames and the upper atmosphere are then discussed.

Introduction

The major source of iron in the earth's upper atmosphere is the ablation of the approximately 120 tonnes of interplanetary dust that enters the atmosphere each day.[1] This process gives rise to a layer of atomic Fe between *ca.* 80 and 95 km that is global in extent, with a peak concentration of *ca.* 2×10^4 atom cm^{-3} around 85 km.[1,2] The layer can be observed by lidar (laser radar) operating by resonance fluorescence on the atomic Fe transition at 372.0 nm [$Fe(z^5D_4^O - a^5D_4)$], providing a probe of the physics and chemistry of an atmospheric region that is otherwise quite inaccessible.[1,2] Indeed, a very recent development is to monitor the relative populations of the $^5D_4$ and $^5D_3$ multiplets of atomic Fe using a two-colour lidar, from which the Boltzmann temperature profile can be determined.[3]

Our understanding of the chemistry that controls the characteristic features of the Fe layer has come from laboratory studies of the relevant reactions, combined with atmospheric modelling.[1,2] Fig. 1 is a schematic diagram of this chemistry. Ion–molecule chemistry governs the topside of the layer above 95 km. Below this altitude, neutral chemistry becomes important. We have shown previously[4,5] that atomic Fe reacts at essentially every collision with O_3 to yield FeO. FeO can react further with O_3 to produce FeO_2, or recombine with O_2, H_2O or CO_2 to form FeO_3, $Fe(OH)_2$ or $FeCO_3$, respectively. However, the recombination of FeO and CO_2 is too slow and $FeCO_3$ is too weakly bound for it to be an important mesospheric species.[5]

The next step in unravelling the atmospheric chemistry of iron is therefore to identify which of the oxides and hydroxides
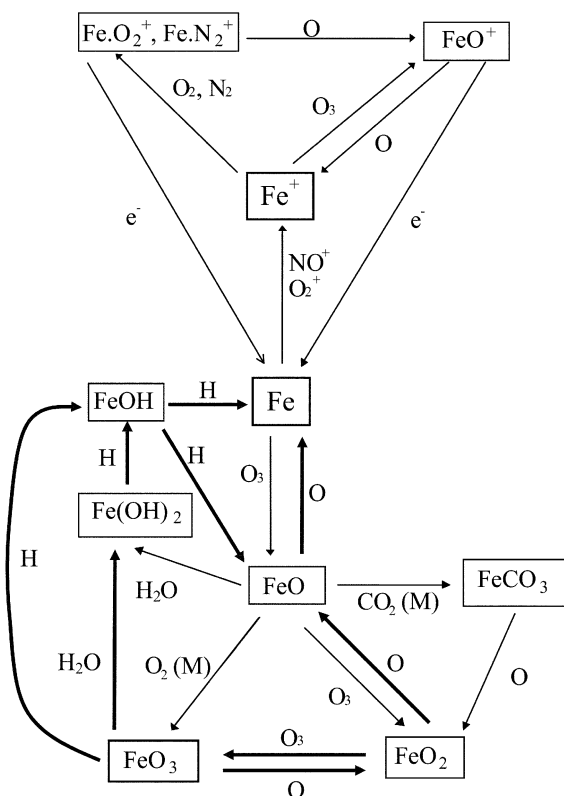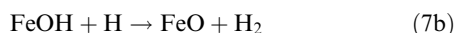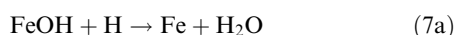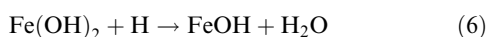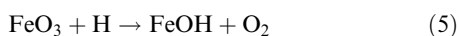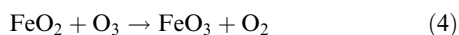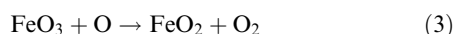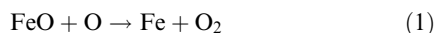

Fig. 1 A schematic diagram of the chemistry of meteor-ablated iron in the upper mesosphere, adapted from ref. 2.

in Fig. 1 is relatively stable with respect to reaction with atomic O and H, and hence provides a substantial reservoir for iron below the Fe layer (O and H are the most abundant reducing agents in the upper mesosphere, in the sense that they convert metallic compounds back to metal atoms). It should be noted that the Fe layer has a very sharp underside gradient, where the concentration changes by nearly an order of magnitude in a kilometre.[6] The steep gradient indicates that the recycling of iron between Fe and its reservoir species must take place on a time-scale of a few hours at most.[6] Of course, below 80 km where the concentrations of O and H fall off by orders of magnitude, these reservoir species are likely to polymerise into so-called meteoric "smoke", nanometre-sized particles that eventually drift down into the stratosphere.[7] Indeed, stratospheric particles of meteoric origin are usually rich in the mineral goethite [Fe(O)OH].[8]

In this paper we will describe kinetic studies of the following reactions, using a novel technique where a pulsed laser ablation source of Fe atoms was coupled to a fast flow tube:

$$FeO + O \rightarrow Fe + O_2 \qquad (1)$$

$$FeO_2 + O \rightarrow FeO + O_2 \qquad (2)$$

$$FeO_3 + O \rightarrow FeO_2 + O_2 \qquad (3)$$

$$FeO_2 + O_3 \rightarrow FeO_3 + O_2 \qquad (4)$$

$$FeO_3 + H \rightarrow FeOH + O_2 \qquad (5)$$

$$Fe(OH)_2 + H \rightarrow FeOH + H_2O \qquad (6)$$

$$FeOH + H \rightarrow Fe + H_2O \qquad (7a)$$

$$FeOH + H \rightarrow FeO + H_2 \qquad (7b)$$

The production of these iron-containing species from atomic Fe in the upstream section of the flow tube inevitably resulted in a complex chemical system, from which the rate coefficients were essentially measured *relative* to absolute rate coefficients for Fe and FeO determined previously. This required the use of a full kinetic model including diffusive loss on the flow tube walls of the relevant species. In some cases, two rate coefficients had to be fitted simultaneously to the experimental data.

It should be noted that none of these reactions appear to have been studied directly. However, the reverse of reaction (1) is endothermic by *ca.* 91 kJ mol^{-1}, and has been investigated at high temperatures;[9,10] by invoking detailed balance we have shown that reaction (1) is likely to be close to the collision frequency.[4] During the course of the present study we established that reaction (1) is indeed fast, and reaction (2) is somewhat slower. However, reaction (3) was found to be extremely slow, which focused attention on FeO$_3$ as a likely

mesospheric reservoir for iron. We therefore studied its formation from the reaction of FeO$_2$ with O$_3$ (reaction (4)), and its reaction with H [reaction (5)].

Estimates for the rate coefficients k_2, and k_6 and k_7 at high temperatures have been derived from modelling the behaviour of iron seeded into flames.[11,12] Indeed, it has been known for more than three decades that compounds such as iron pentacarbonyl are very effective flame inhibitors.[12] Jensen and Jones[11] originally proposed that inhibition occurred through the removal of the major flame radicals H and OH by a catalytic cycle involving FeO, FeOH and Fe(OH)$_2$. This mechanism received further attention in a recent modelling study by Rumminger *et al.*,[12] which was motivated by the requirement to find alternative fire retardants to the halons. However, achieving a detailed understanding of the inhibition chemistry has been hindered by the lack of kinetic studies of the elementary reactions involved.[12]

Experimental

Reactions 1–7 were studied in the fast flow tube shown schematically in Fig. 2. The tube was constructed from stainless steel, with an internal diameter of 37.5 mm and a length of 730 mm from the laser ablation source at the upstream end, through the reaction zone, to the spectroscopic detection cell (a commercial stainless steel 6-way cross). Downstream of the cross piece was a quadrupole mass spectrometer which sampled along the cylindrical axis of the tube through a 100 μm orifice in the centre of a skimmer cone. The different sections of the tube were coupled together with commercial 70 mm "Conflat" flanges with copper gaskets. The carrier gas (N$_2$) flow entered the tube upstream of the ablation source, and exited through a throttle valve to a booster/rotary pump combination, providing a volume displacement rate of 110 l s^{-1}.

The main carrier gas and reagent gas flows were set by calibrated electronic mass flow controllers. The temperature and total pressure in the reaction zone upstream of the spectroscopic cell were measured with a chromel–alumel thermocouple and a capacitance manometer, at the points shown in Fig. 2. Sub-ambient temperatures down to 209 K were achieved by cooling the flow tube walls around the reaction zone with dry ice; alternatively, heating tape was wrapped around the tube to heat the gas up to a maximum temperature of 610 K. The tube was normally operated with a total mass flow rate of 2000 sccm and a pressure of 1.50 Torr, so that the plug flow velocity in the tube was 1720 cm s^{-1} at 294 K.

The source of Fe-containing species in the flow tube was the pulsed ablation of a pure iron rod, using a Nd : YAG laser
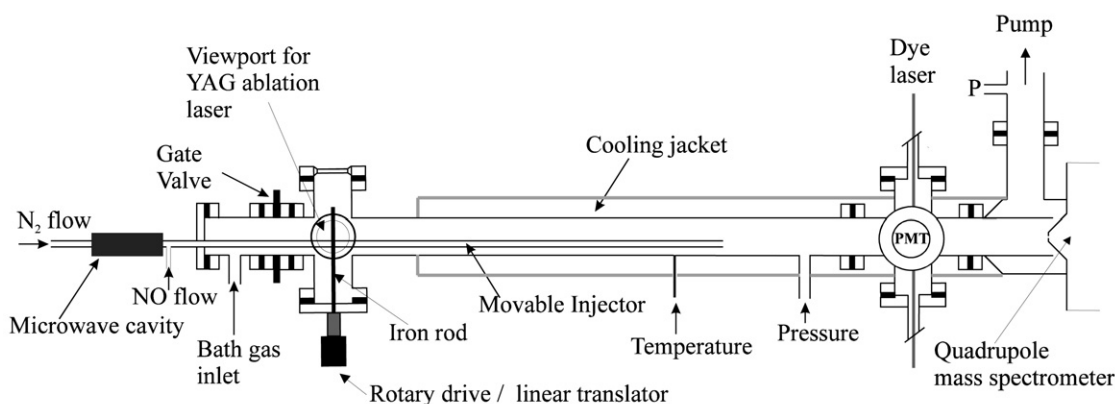

Fig. 2 A schematic drawing (approximately to scale) of the fast flow tube employed to study the reactions of iron-containing species produced by pulsed laser ablation (PMT = photomultiplier tube).

($\lambda = 532$ nm, pulse energy = 22–31 mJ, repetition rate = 8 Hz). The rod was coupled to a stepper motor *via* a vacuum feedthrough in a side-arm of the flow tube (Fig. 2), so that the rod could be rotated (2–4 Hz) and also translated slowly. Rotation ensured that a fresh surface of the rod was presented to each successive laser shot, in order to keep the resulting pulses of ablated Fe as uniform as possible. The iron rod was long enough (*ca.* 5 cm) to project across the central axis of the tube. The laser was loosely focused onto the rod through an orthogonal side-arm, so that the point of ablation was in the centre of the flow tube.

The pulse of Fe atoms was then entrained in the N_2 carrier gas and transported downstream to the spectroscopic cell, where the Fe was detected by laser induced fluorescence (LIF) at 248.327 nm Fe($x^5F^0_5 \leftarrow a^5D_4$, $A_{nm} = 4.9 \times 10^8$ s^{-1}) using a pulsed dye laser. A few experiments to record the profile of the pulse were performed using an iron hollow cathode lamp to stimulate resonance fluorescence, which was captured by time-resolved photon counting. Finally, the absolute concentration of Fe in the pulse was measured by resonance absorption. In this configuration the radiation from the hollow cathode lamp was focused through the spectroscopic cell, transversely to the flow, and into a fibre optic which was coupled to a spectrometer with a cooled CCD detector. The camera shutter was opened for *ca.* 10 ms to coincide with the passage of the peak of the Fe pulse through the spectroscopic cell. This arrangement, with the hollow cathode lamp switched off, also allowed emissions from electronically excited Fe atoms in the pulse to be observed and spectrally resolved.

The Fe-containing reactant species (FeO, FeO_2, *etc.*) were produced *in situ* from atomic Fe *via* the addition of appropriate oxidants (NO_2, O_2) just downstream of the ablation cell. Further downstream in the reaction zone, reactants such as O, H and O_3 were added through a sliding silica injector. Note that this injector was positioned along the wall of the tube, rather than along the cylindrical axis, in order to minimize the loss of Fe-containing species by deposition, and because the iron rod in the ablation source crossed the central axis of the tube. The opening at the tip of the injector was designed to direct the reactants towards the centre of the flow tube, ensuring more rapid mixing into the carrier gas flow.

Atomic O was prepared by microwave discharge of N_2, followed by immediate titration with NO. The reaction NO + N → O + N_2 went essentially to completion in the first few cm of the injector, so that the end point of the titration could be judged by visual inspection of the change in chemiluminescence from blue (emission from NO*) to bright green (emission from NO_2*). The O atom concentration at the point of injection into the main flow was measured by the standard titration with NO_2.[13] For this purpose a second photomultiplier tube was coupled to the 6-way cross of the spectroscopic cell in order to measure the resulting chemiluminescence through an interference filter (555 nm, FWHM = 10 nm). For [O] $< 5 \times 10^{12}$ cm^{-3}, when titration with NO_2 was not possible, the *relative* [O] was measured by adding sufficient NO just above the spectroscopic cell to generate an observable chemiluminescence signal from O + NO → NO_2*. This signal was calibrated against the signal generated from a large [O] which could be measured absolutely by titration with NO_2. This procedure enabled [O] to be measured down to 5×10^{10} cm^{-3}. The diffusional loss of O to the walls of the flow tube was determined by monitoring the relative change in [O] as the injector was moved along the tube.

Atomic H was prepared by the microwave discharge of H_2, and absolute [H] was determined by titration with NO_2 and mass spectrometric detection of the change in NO_2, a technique that we have described previously.[14] The relative [H] was measured by adding NO just above the spectroscopic cell and monitoring chemiluminescence from H + NO → HNO* through a cut-on filter at $\lambda > 645$ nm.

N_2 carrier gas (99.9992% pure) was purified by passage through a trap containing molecular sieve at 77 K. NO (99%) was purified by passage through molecular sieve at 153 K to remove any traces of NO_2. NO_2 (99.5%) was purified by repeated distillation from 196 to 77 K before use. H_2O was generated by bubbling N_2 through Milli-Q water at 298 K. O_3 was prepared by flowing O_2 through an ozoniser. The resulting O_3/O_2 mixture was trapped on silica gel at $-119\,°C$, and purified by slow warming under vacuum to give a *ca.* 30% mixture, which was then diluted with N_2 in a 12 l glass bulb. The concentration of O_3 was monitored by optical absorption of a low-pressure mercury lamp at 253.7 nm ($\sigma = 1.143 \times 10^{-17}$ cm^2) in a 1 m path cell that was placed upstream of the sliding injector that entered the flow tube. The resulting concentrations were then corrected for the significant pressure drop between the absorption cell and the flow tube, which was a function of the relative flow rates.

Results

Fig. 3 illustrates a sequence of pulses of atomic Fe recorded at constant pressure but different flow velocities, and hence flow times, between the ablation source and the downstream spectroscopic cell. An important advantage to using the pulsed source of metal atoms is that the flow time down the tube is measured directly. This technique contrasts with the usual situation where a continuous metal source such as an oven is employed,[15] and the flow time is calculated using an approximate solution to the continuity equation describing first-order kinetics in a cylindrical flow tube under parabolic flow conditions.[15] Fig. 3 shows that at longer flow times the pulses become broader because of axial diffusion, and exhibit a decrease in both pulse height and pulse area because of radial diffusion and deposition of Fe to the walls. Fig. 4 shows that the natural logarithm of either the pulse height or the pulse area, *versus* flow time, are linear with essentially identical slopes. This behaviour arises because the loss of Fe on the walls is a first-order process, and also indicates that either the pulse height or area can be used as a measure of [Fe]. Note that the loss process is inversely proportional to pressure:the slopes of the 2 Torr plots are 84 ± 8 s^{-1}, compared with 154 ± 16 s^{-1} for the 1 Torr plots. The measurements confirm that the loss process is diffusion controlled, which would be the case if uptake of Fe on the walls occurred with near unit efficiency.[15] The diffusion coefficient for Fe in N_2, D_{Fe}, can then be obtained from the expression
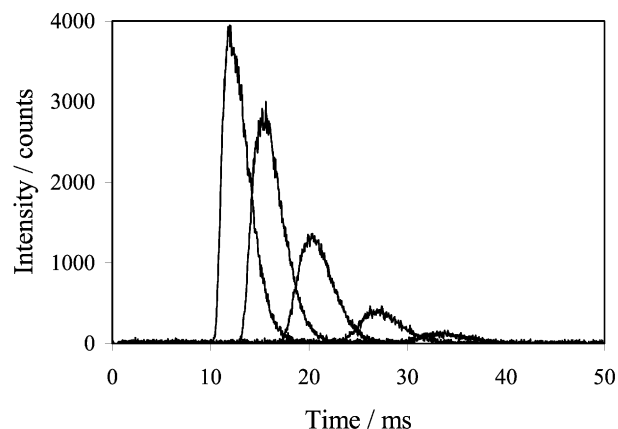
$$D_{Fe} = k'r^2/3.67 \qquad (I)$$

Fig. 3 A sequence of Fe pulses, measured by time-resolved resonance fluorescence at 248.327 nm Fe($x^5F^0_5 \leftarrow a^5D_4$), at different times down the flow tube.
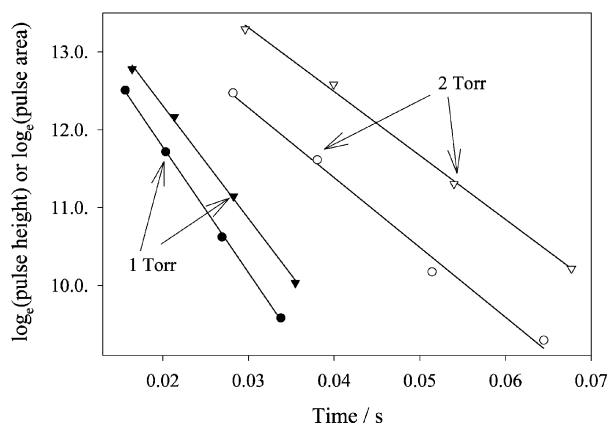
Fig. 4 The logarithm of the Fe pulse maximum ($\bigcirc$ and $\bullet$), or pulse area ($\triangledown$ and $\blacktriangledown$), plotted against the centroid time of the pulse, at two different total pressures.

where k' is the measured first-order loss rate and r is the tube radius, which yields $D_{Fe} = 84^{+19}_{-11}$ Torr cm^2 s^{-1}. This equation arises from the approximate solution to the continuity equation describing first-order kinetics in a cylindrical flow tube, under parabolic flow conditions.[15,16]

The absolute Fe(a ^{5}D) density at the downstream detection point was measured to be *ca.* 1×10^{10} cm^{-3} at the peak of the largest Fe pulses used in this study (observed with the shortest flow times). This concentration was determined using resonance absorption at 248.3 nm (see Experimental), together with an absorption cross section of 7.34×10^{-12} cm^2 molecule^{-1} computed from the transition probability $A_{nm} = 4.9 \times 10^8$ s^{-1} (statistical weights $g_n = 9$, $g_m = 11$).[17] The wall loss rates determined above can be used to extrapolate the Fe density to the upstream section of the tube; [Fe] $\approx 10^{11}$ cm^{-3} close to the ablation source. In the section of the tube where the kinetic measurements were performed, the total density of all Fe-containing species was therefore at least 2 orders of magnitude less than the concentrations of reactants such as O, O$_3$ and H.

Excited states of Fe

A significant fraction of the Fe atoms produced in the laser ablation source were in excited electronic states, and some of these were metastable, persisting for at least 1 ms in 1.5 Torr of N$_2$. There were two pieces of evidence for the existence of metastable states. First, emissions from excited states of Fe were observed with the spectrometer/CCD as the ablation pulse passed the downstream detection point. Prominent transitions were 372 nm [Fe(z^{5}F$^0 \rightarrow$ a^{5}D$_4$)], 386 nm [Fe(z^{5}D$^0 \rightarrow$ a^{5}D$_4$)], 423 nm [Fe(e^{7}D$_J \rightarrow$ z^{7}D$^0_{3,4,5}$)], 491 nm [Fe(e^{7}D$_J \rightarrow$ z^{7}F$^0_{4,5,6}$)] and 524 nm [Fe(e^{7}D$_J \rightarrow$ z^{7}P$^0_{2,3,4}$)].[18] These observations indicate that the e^{7}D state, which lies 5.3 eV above the a^{5}D$_4$ ground state,[18] is either metastable or a decay product from a higher lying metastable state. Fe(a^{5}P$_J$), Fe(a^{3}P$_J$) and Fe(z^{7}D^0_J) are three metastable states that could also be formed during the ablation process. They are 2.18, 2.28 and 2.40 eV above the ground state and thus close to resonant with a 532 nm photon (2.33 eV), and have radiative lifetimes of 4.0, 2.5 and 6.9×10^{-4} s, respectively.[18] There does not appear to be any information regarding the quenching of these higher-lying Fe states by N$_2$ (Mitchell and Hackett[19] studied quenching of states up to Fe(a^{3}F$_3$), which is only 1.49 eV above the ground state). Therefore, in the absence of further information we simply label these possible metastable states collectively as Fe*.

The second piece of evidence for Fe* was that the addition of O$_2$ or N$_2$O through the sliding injector reduced

the concentration of ground state Fe(a^{5}D$_4$) observed by LIF at the downstream detection point, even though these oxidants react very slowly with ground-state Fe(a^{5}D$_J$) at 300 K.[20,21] This observation implies that Fe* was removed relatively rapidly by these reactants, rather than being quenched by N$_2$ to Fe-(a^{5}D$_J$) as the pulse travelled down to the detection point. Indeed, by varying [O$_2$] it was possible to show that Fe* reacted with O$_2$ with a rate coefficient of approximately 1×10^{-11} cm^3 molecule^{-1} s^{-1} at 300 K. This rate coefficient is close enough to the collision frequency at a bath gas pressure of only 1 Torr that we conclude that the reaction involves abstraction to form FeO, rather than recombination to FeO$_2$.[21] Since the reaction between Fe(a^{5}D$_J$) and O$_2$ is endothermic by 0.95 ± 0.12 eV,[4] any of the metastable states discussed above would be sufficiently energetic to react with O$_2$.

The quenching by N$_2$ of Fe* to Fe(a^{5}D$_J$) was measured by adding a large concentration of O$_2$ through the sliding injector to remove all Fe* downstream of the injection point. The injector was then moved down the tube to increase the upstream time during which Fe* was quenched by N$_2$. Analysis yielded k(Fe* + N$_2 \rightarrow$ Fe(a^{5}D$_J$) + N$_2$, 294 K) = 2.8×10^{-15} cm^3 molecule^{-1} s^{-1}. Interestingly, Fe* did not appear to react with H$_2$O ($k < 1 \times 10^{-13}$ cm^3 molecule^{-1} s^{-1}), even though only 1.6 ± 0.3 eV of Fe* excitation energy would be required for FeOH formation to become exothermic.

Kinetic measurements

The kinetics of reactions (1)–(7) were studied by converting atomic Fe to FeX (the Fe-containing molecule of interest), in the upstream section of the tube; injecting the second reactant (O, H, *etc.*) further downstream; and then observing the resulting increase in the atomic Fe signal as FeX was converted back to Fe. The important quantity derived is the ratio of the observed increase in Fe to the amount of Fe originally converted to FeX, hereafter termed the *fraction of Fe recovered* and denoted as %Fe. In all these experiments, the relative Fe concentrations were measured by LIF at the pulse peak.

With the exception of reaction (4), the rate coefficients were determined *relative* to the absolute rates at which Fe was converted to FeX (described in detail below). FeX was also usually converted back to Fe *via* an intermediate (*e.g.* FeO$_2$ + O $\rightarrow$ FeO + O$_2$, FeO + O $\rightarrow$ Fe + O$_2$). Furthermore, all the Fe-containing species and reactants such as O and H were lost efficiently on the stainless steel walls. In order to characterise this complex system, it was essential to use a full model of the flow tube describing all the processes that occurred between the ablation source and the downstream detection point.

Table 1 lists the processes, in addition to reactions (1)–(7), that were included in the model (note that only a subset of this scheme was applied when a particular reaction was studied). The ordinary differential rate equations were integrated using a 4th order Runge–Kutta routine with variable step size.[25] Stability tests showed that the variation in total iron down the tube was less than 1 part in 10^6. The model incorporated the effect of flow velocity changes when significant reactant gas flows were added downstream of the ablation source. Temperature changes between heated or cooled sections of the flow tube were represented by discrete temperature jumps at a point which was half the diffusional mixing distance from the edge of the heated or cooled section. The addition of reactants was also assumed to occur over a mixing distance downstream of the point of injection, given by[26]

$$z = \frac{\nu\, r^2\, P}{3.67\, D} \left(\frac{T}{300\ \text{K}}\right)^{1.83} \tag{II}$$

Table 1 Rate coefficients used to model the flow tube chemistry

	Reaction	Rate coefficient[a]	Source[b]
8	$Fe + NO_2 \rightarrow FeO + NO$	$4.84 \times 10^{-10} e^{-313/T}$	1
9	$FeO + NO_2 \rightarrow FeO_2 + NO$	$5.04 \times 10^{-10} e^{-438/T}$	1
10	$Fe + O_2 (+N_2) \rightarrow FeO_2$	$4.34 \times 10^{-30} e^{-2038/T}$	2
11	$Fe + O_3 \rightarrow FeO + O_2$	$3.44 \times 10^{-10} e^{-146/T}$	3
12	$FeO + O_3 \rightarrow FeO_2 + O_2$	$2.94 \times 10^{-10} e^{-174/T}$	4
13	$FeO + O_2 (+N_2) \rightarrow FeO_3$	$3.86 \times 10^{-30} (T/300\ K)^{0.50}$	4
14	$Fe + NO (+N_2) \rightarrow FeNO$	2.3×10^{-32}	5
15	$FeO + H_2O (+N_2) \rightarrow$ $Fe(OH)_2$	$8.23 \times 10^{-29} (T/300\ K)^{-1.16}$	4
16	$FeO + H_2 \rightarrow Fe + H_2O$	0	4
17	$Fe^* + O_2 \rightarrow FeO + O$	1×10^{-11} at 294 K	7
18	$Fe^* + N_2 \rightarrow Fe + N_2$	2.8×10^{-15} at 294 K	7
19	$O + NO (+N_2) \rightarrow NO_2$	$1.0 \times 10^{-31} (T/298\ K)^{-1.6}$	6
20	$O + NO_2 \rightarrow NO + O_2$	$6.5 \times 10^{-12} e^{120/T}$	6
21	Diffusion of Fe	$84 (T/300\ K)^{1.83}$	7
22	Diffusion of FeO	$115 (T/300\ K)^{1.83}$	8
23	Diffusion of FeO_2	$149 (T/300\ K)^{1.83}$	8
24	Diffusion of FeO_3	$149 (T/300\ K)^{1.83}$	8
25	Diffusion of $Fe(OH)_2$	$149 (T/300\ K)^{1.83}$	8

[a] Units: bimolecular reactions (cm^3 molecule^{-1} s^{-1}); termolecular reactions (cm^6 molecule^{-2} s^{-1}); diffusion coefficients (Torr cm^2 s^{-1}). [b] 1. Ref. 20. 2. Ref. 21. 3. Ref. 4. 4. Ref. 5. 5. Ref. 22. 6. Ref. 23. 7. Measured in this study. 8. Calculated from theory (see text).

where v is the gas velocity, r the radius of tube, T the temperature, P the pressure in Torr and D the diffusion coefficient at 300 K of the reactant gas in N_2.

The diffusion coefficient of Fe in N_2, D_{Fe}, was measured at 299 K (see above). The values of D_{FeO} and D_{FeO_2} listed in Table 1 were then fitted to the experimental data at 299 K, as described below. All of these diffusion coefficients can also be estimated from a formalism[24] we have used previously for Na-containing species.[16] The long-range dispersion and dipole-induced dipole forces between FeX and N_2 were calculated using the polarizabilities, ionization energies and dipole moments listed in Table 2. The resulting diffusion coefficients (Table 2) are very similar: Fe is more polarizable than FeO or FeO_2, but does not have a dipole moment. A comparison with the measured values in Table 1 shows excellent agreement for D_{FeO}. The calculated D_{FeO_2} is 20% lower than the measured value; this would be explained if the polarizability of FeO_2 were ca. 50% that estimated from quantum calculations (see below). The calculated D_{Fe} is 44% higher than the measured value (18% at the upper end of the uncertainty in the measured D_{Fe}). This discrepancy most likely indicates that the uptake coefficient of Fe on the stainless steel walls is below unity, probably as a result of a protective coating of iron oxides and hydroxides (in a nearly identical experiment, yet to be published, B. J. Murray and J. M. C. Plane observed a higher uptake rate of Fe on clean Pyrex glass.[27])

The diffusion coefficients of FeO_3 and $Fe(OH)_2$ were then set equal to D_{FeO_2}. Note that the model is actually sensitive to the difference $D_{FeX} - D_{Fe}$, rather than the absolute values of the

Table 2 Theoretical calculations of the diffusion coefficients of Fe species in N_2

Species	Dipole moment[a]	Polarizability[b]	Ionization energy[c]	Diffusion coefficient[d]
Fe	0	8.4×10^{-24} [e]	7.9[f]	120
FeO	4.7[f]	5.7×10^{-24} [g]	8.9[f]	119
$FeO_2(^5B_2)$	4.0[g]	5.4×10^{-24} [g]	9.5[g]	118

[a] Debye. [b] cm^3. [c] eV. [d] Torr cm^2 s^{-1}, at 300 K. [e] Ref. 17. [f] Ref. 28. [g] Calculated at the B3LYP/6-311+g(2d,p) level of theory.

diffusion coefficients. We have assumed a $T^{1.83}$ dependence[16,24] for all the diffusion coefficients used in the model.

$FeO + O$ and $FeO_2 + O$ [reactions (1) and (2)]

In order to study reaction (1), a clean source of FeO would have been desirable but was difficult to achieve in practice. The reactants that oxidise Fe to FeO rapidly at ambient temperature are O_3 and NO_2.[4,20] Unfortunately, FeO also reacts with these oxidants to form FeO_2,[5,20] which is oxidised further by O_3 (but not NO_2) to FeO_3, as shown below. N_2O is probably a cleaner oxidant, but the reaction $Fe + N_2O$ has a large activation energy[29] and temperatures of over 700 K would have been required in the upstream section of the flow tube. Therefore, the best compromise was to use NO_2 and measure the rate constants $k_1(FeO + O)$ and $k_2(FeO_2 + O)$ simultaneously.

Fig. 5 illustrates a model simulation of a typical experiment, showing [Fe] as a function of flow time between the ablation source and detection point. In the absence of NO_2, [Fe] decays exponentially due to diffusion to the walls and irreversible deposition, yielding the observed signal $[Fe]_0$ at the detection point. When NO_2 is then added 6 ms downstream, the decay becomes much more pronounced leading to a reduction in the observed Fe signal by ca. 2 orders of magnitude. This background signal is termed $[Fe]_{NO_2}$. Finally, when atomic O is injected 22 ms downstream, the Fe signal recovers by more than 1 order of magnitude, giving the measured signal $[Fe]_{NO_2+O}$. The fraction of Fe recovered, %Fe, is then given by $([Fe]_{NO_2+O} - [Fe]_{NO_2})/([Fe]_0 - [Fe]_{NO_2})$. Fig. 6a is a mesh plot showing how this fraction varies as a function of $[NO_2]$ and [O], at 299 K. Similar data sets were acquired at four other temperatures between 209 and 381 K. It should be noted that because small concentrations of NO_2 had to be employed ($<10^{12}$ cm^{-3}) and this gas is difficult to control precisely at these levels, $[NO_2]$ was actually calculated from the observed loss of Fe (before O was added) using $k_8(Fe + NO_2)$ from Plane and Rollason.[20]

The best fit values of k_1 and k_2 at each temperature were found using a grid search and least-squares procedure. Trial values of k_1 and k_2 were selected and input to the model, which then calculated %Fe for each of the N combinations of $[NO_2]$ and [O] used in the experiments at a particular temperature.
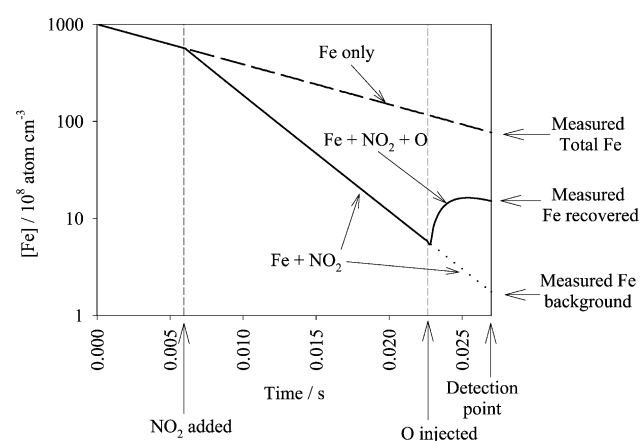

Fig. 5 Plot of modelled [Fe] as a function of time down the flow tube from the ablation source, during a typical experiment to study the reactions of FeO and FeO_2 with O at 294 K. The (relative) Fe concentration, measured at the downstream point, is shown for comparison. A sequence of three different reagent combinations was used: (1) no reagents, labelled Fe only and giving rise to the measured total Fe; (2) NO_2 added upstream, labelled $Fe + NO_2$ and yielding the measured Fe background; and (3) O injected downstream, labelled $Fe + NO_2 + O$, which produces the measured Fe recovered.
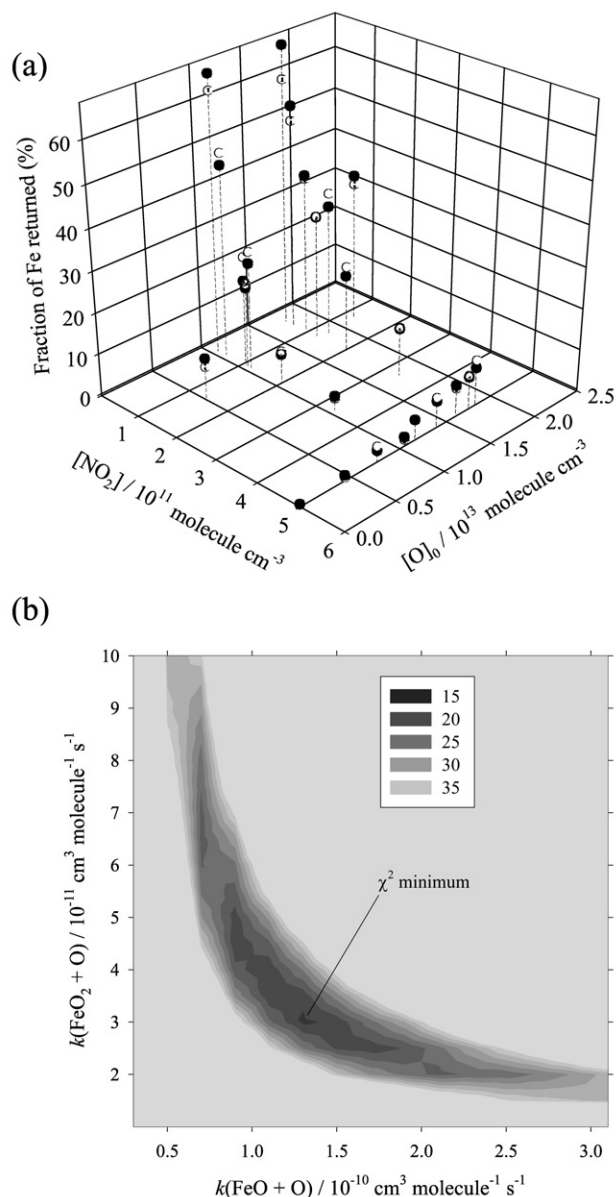
(a)

(b)

Table 3 Estimates of k_1 and k_2 from χ^2 minimisation over a range of temperature

T/K	χ^2_{min}	χ^2_B	v	Q	$k_1(FeO + O)/$ cm^3 s^{-1}	$k_2(FeO_2 + O)/$ cm^3 s^{-1}
209	6.9	10	8	0.55	$8^{+10}_{-4} \times 10^{-11}$	$1.1^{+0.8}_{-0.3} \times 10^{-11}$
249	3.0	6	4	0.56	$9.5^{+7.5}_{-3.5} \times 10^{-11}$	$9.5^{+6}_{-3.5} \times 10^{-12}$
299	16.9	25	21	0.72	$1.30^{+1.4}_{-0.6} \times 10^{-10}$	$3.0^{+5.2}_{-1.0} \times 10^{-11}$
341	10.9	14	12	0.54	$1.6^{+0.9}_{-0.7} \times 10^{-10}$	$2.0^{+1.4}_{-0.6} \times 10^{-11}$
381	12.5	15	13	0.49	$1.9^{+0.9}_{-0.6} \times 10^{-10}$	$3.4^{+1.6}_{-1.3} \times 10^{-11}$

of [NO$_2$] and [O] employed. The average difference between model and experiment is only 1.9%.

The confidence limits of k_1 and k_2 were found by evaluating the chi-squared boundary, χ^2_B.[25] This quantity is the sum of squares of the total normalised errors for each data point, which is equal in this case to N, the number of data points in the set at a particular temperature.[30] Table 3 lists the values of χ^2_{min} and χ^2_B, as well as Q, the probability that the number of degrees of freedom, v ($= N - M$, where M is the number of fitted parameters), is greater than χ^2_{min} by chance.[25] In all cases Q is close to unity, indicating that the model is essentially a correct description of the experiment. The confidence limits for k_1 and k_2 at each temperature in Table 3 were then increased to take account of two significant sources of systematic error: the absolute [O] at the point of injection ($\pm 8\%$), and the rate of wall loss of atomic O ($\pm 12\%$).

Weighted linear regression fits through the Arrhenius plots for reactions (1) and (2) illustrated in Fig. 7 yield:

$$k_1(209 - 381 \text{ K})$$
$$= 4.6^{+2.6}_{-1.6} \times 10^{-10} \, e^{-(350 \pm 130)/T} \text{ cm}^3 \text{ molecule}^{-1} \text{ s}^{-1}$$

$$k_2(209 - 381 \text{ K})$$
$$= 1.4^{+0.8}_{-0.5} \times 10^{-10} \, e^{-(580 \pm 120)/T} \text{ cm}^3 \text{ molecule}^{-1} \text{ s}^{-1}$$

FeO$_3$ + O [reaction (3)]

Initially, FeO$_3$ was produced in the flow tube by adding NO$_2$ and O$_2$ simultaneously, *i.e.* reaction (8) followed by (13). However, a significant quantity of FeO$_2$ was also unavoidably produced by reaction (9), resulting in the rapid reappearance of Fe when O was injected downstream. This problem was circumvented by adding only O$_2$ to the Fe pulse
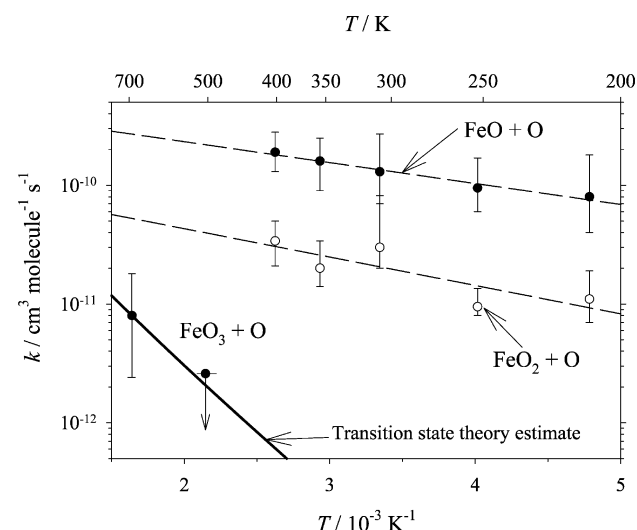
Fig. 6 (a) Plot of the fraction of Fe recovered as a function of [NO$_2$] and [O]$_0$ (the atomic O concentration immediately downstream of the point of injection). Measured data points ($\bullet$) are compared with the optimised model ($\circ$) at 299 K. (b) Contour plot of χ^2 [eqn. (III)] as a function of $k(FeO + O)$ and $k(FeO_2 + O)$ at 299 K.

The sum of squares of the differences between the experimental and modelled %Fe , weighted by the inverse square of the uncertainty in the experimental %Fe, yields χ^2:

$$\chi^2 = \sum_{i=1}^{N} (\%Fe_{expt,i} - \%Fe_{model,i})^2 / (\text{uncertainty in } \%Fe_{expt,i})^2$$

(III)

χ^2 was calculated over a grid of k_1 and k_2 values. The minimum on the resulting 3-dimensional χ^2 surface corresponds to the best fits to k_1 and k_2. An example of such a surface, showing a clear χ^2 minimum, is illustrated in Fig. 6(b). The largest number of measurements of %Fe, over a wide range of [NO$_2$] and [O], was made at 299 K. Hence this data set was also used to find the values of D_{FeO} and D_{FeO_2} in the model that gave a global χ^2 minimum. Fig. 5 demonstrates the excellent agreement between the model prediction and the experimental measurements for a single combination of [NO$_2$] and [O]. Fig. 6 (a) shows that the agreement between measured and modelled %Fe remains very satisfactory over the wide range

Fig. 7 Arrhenius plots for the reactions FeO + O, FeO$_2$ and FeO$_3$ + O. The broken lines are regression fits through the data-points; the solid line is a fit of transition state theory (see text).

in the upstream section of the tube, at a point 3 ms flow time downstream of the ablation source where the concentration of metastable Fe was still relatively large. Fe* reacted to form FeO [reaction (17)], followed by recombination with O_2 to produce FeO_3 [reaction (13), Table 1].

Reaction (3) was then studied using the same experimental method as for reactions (1) and (2), by detecting Fe at the downstream detection point after O was added through the sliding injector. k_3 turned out to be very much smaller than k_1 or k_2. Hence, in the sequence of reactions $(3) \rightarrow 2 \rightarrow 1$ that produced Fe from FeO_3, reaction (3) was rate-determining which greatly simplified the analysis. In the model, Fe* was treated as a single excited state of Fe, as it can be assumed that all of the iron at the point of O injection was in the form of Fe or FeO_3. Furthermore, the $Fe(a^5D_4)$ produced in the final step was not re-oxidised by O_2 because reaction (10) is so slow, even up to 610 K, the highest temperature achievable with this flow tube. In fact, no reaction between FeO_3 and O was observed at temperatures up to 466 K ($k_3 < 2.1 \times 10^{-12}$ cm^3 molecule^{-1} s^{-1}), and only an approximate estimate of $k_3 = 8\,^{+10}_{\,-5} \times 10^{-12}$ cm^3 molecule^{-1} s^{-1} was obtained at 610 K. The stated errors include the likely uncertainty in $D_{FeO_3} - D_{Fe}$, and the uncertainties in the model parameters k_{diff} (O), [O], k_1 and k_2. The Arrhenius plot in Fig. 7 for reaction (3), when combined with transition state theory (see below), indicates that this reaction has a substantial activation energy compared with reactions (1) and (2).

FeO$_2$ + O$_3$ [reaction (4)]

This reaction was studied by adding a sufficiently large concentration of NO_2 in the upstream section of the flow tube to produce FeO_2 rapidly by reactions (8) and (9) going essentially to completion in the first half of the tube. An O_3/O_2 mixture in N_2 was then added through the sliding injector. The FeO_2 remaining in the downstream section was monitored by adding a large concentration of O ($ca.\ 2 \times 10^{13}$ cm^{-3}) just upstream of the spectroscopic cell, in order to reduce FeO_2 (but not FeO_3, see above) back to Fe for detection by LIF. Fig. 8a illustrates the fraction of Fe recovered as a function of [O_3], using a fixed injection point at 298 K. This experiment shows that the product of the reaction $FeO_2 + O_3$ is a compound that reacts extremely slowly with O atoms, as was found when producing FeO_3 from the alternative reaction of Fe* and O_2.

The value of k_4 in the flow tube model (Table 1) was then optimised to obtain the very satisfactory fit to the experimental data shown in Fig. 8a. Reaction (4) was studied at two temperatures, yielding $k_4 = (2.27 \pm 0.42) \times 10^{-10}$ and $(2.68 \pm 0.46) \times 10^{-10}$ cm^3 molecule^{-1} s^{-1} at 224 and 298 K, respectively. The corresponding Arrhenius expression is $k_4(224 - 298\ \text{K}) = 4.4\,^{+6.4}_{\,-2.6} \times 10^{-10}\ e^{-(150 \pm 230)/T}$ cm^3 molecule^{-1} s^{-1}. Fig. 8b is an Arrhenius plot comparing the reactions of Fe, FeO and FeO_2 with O_3. The plot shows that all three reactions proceed essentially at the collision number, with very small activation energies.

FeO$_3$, Fe(OH)$_2$ and FeOH + H [reactions (5)–(7)]

FeO_3 was prepared as before by adding O_2 in the upstream section of the flow tube, so that Fe* reacted with O_2 to generate FeO, which then recombined with O_2 [reaction (13), Table 1]. In order to make $Fe(OH)_2$, excess H_2O was added simultaneously in the upstream section. The ratio of [H_2O]:[O_2] was greater than 1.5:1, so that more than 98% of the FeO recombined with H_2O to form $Fe(OH)_2$ by reaction (15), rather than FeO_3. The addition of H through the injector produced a large increase in %Fe from both FeO_3 and $Fe(OH)_2$, as shown in Fig. 9a. In the analysis that follows, we assume that FeOH is produced from FeO_3 [reaction (5)] or $Fe(OH)_2$ [reaction (6)], and the observed Fe by reaction (7). Note that this reaction
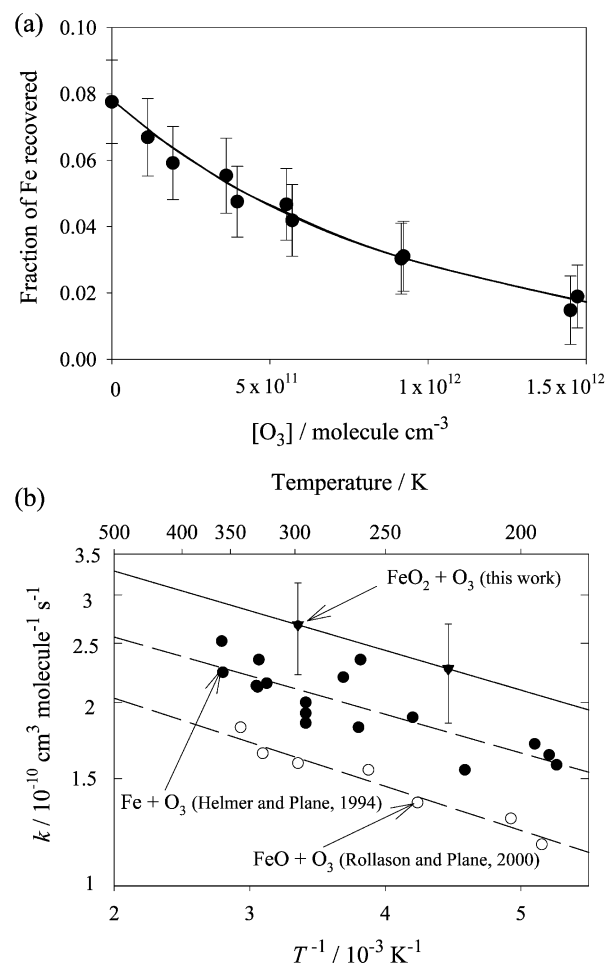

(a)

(b)

Fig. 8 (a) Plot of the fraction of Fe recovered at the end of the flow tube as a function of [O_3]. Atomic O was injected just above the detection point to generate Fe from any FeO_2 remaining during a study of the reaction $FeO_2 + O_3 \rightarrow FeO_3 + O_2$ at 294 K. (b) Arrhenius plots for the reactions $FeO_2 + O_3$, $Fe + O_3$ (ref. 4) and $FeO + O_3$ (ref. 5).

has two channels. If reaction (7b) ($FeOH + H \rightarrow FeO + H_2$) is the dominant channel at 294 K, then the reaction $FeO + H \rightarrow Fe + OH$ must proceed at close to the collision number, as discussed below.

The production of Fe from FeO_3 via the reaction sequence $(5) \rightarrow (7)$ involves H in both steps. The same applies to the formation of Fe from $Fe(OH)_2$ via $(6) \rightarrow (7)$. The only way to find the rate determining step in either of these reaction sequences, and hence uncouple their respective rate coefficients, would be to monitor FeOH directly—unfortunately, no spectroscopic data on FeOH appears to exist. Instead, we have utilised the results of the most recent flame study by Rumminger et al.[12] Those authors found that $k_6 = 3.3 \times 10^{-10}\ e^{-302/T}$ cm^3 molecule^{-1} s^{-1} and $k_7 = 2.5 \times 10^{-10}\ e^{-805/T}$ cm^3 molecule^{-1} s^{-1}, over the temperature range 1800 to 2200 K. These rate coefficients then extrapolate to 1.2×10^{-10} and 1.6×10^{-11} cm^3 molecule^{-1} s^{-1} at 294 K, respectively, so that reaction (7) should be the rate determining step in the sequence $(6) \rightarrow (7)$. If we assume this to be the case, then the best fit of the flow tube model to the two experimental points in Fig. 9a yields $k_7 = (1.3 \pm 0.3) \times 10^{-11}$ cm^3 molecule^{-1} s^{-1}, where the quoted uncertainty includes the experimental errors in the relative amount (percentage) of Fe returned by reaction, %Fe, and in the concentration of H atoms. This result is in good agreement with the estimate of 1.6×10^{-11} cm^3 molecule^{-1} s^{-1} from Rumminger et al.[12] (it should be noted that it was based on the earlier work of Jensen and Jones,[11] but with the pre-exponential factor of k_7 increased by a factor of 5).
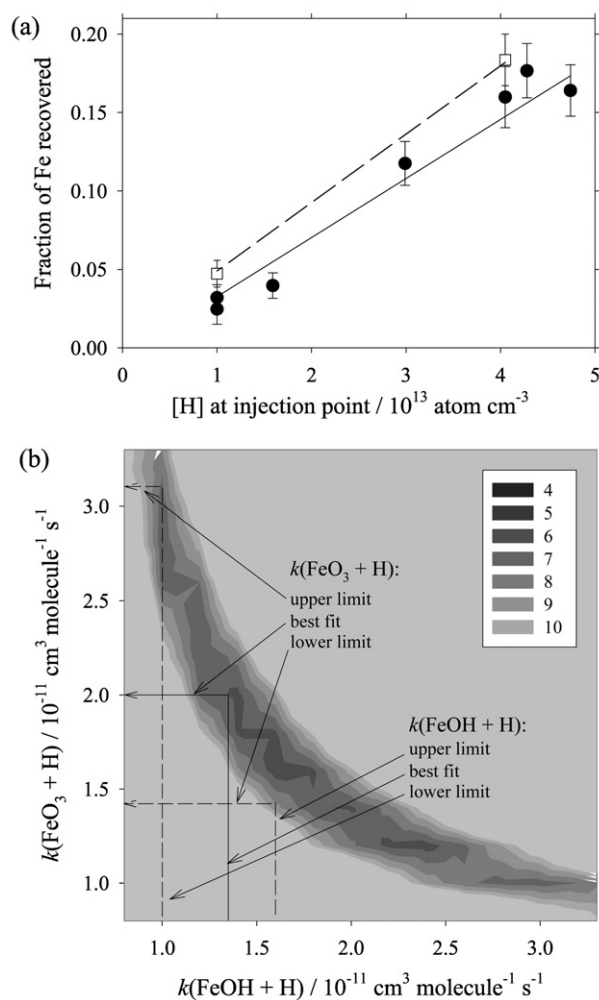
Fig. 9 (a) Plots of the fraction of Fe recovered at the end of the flow tube as a function of injected atomic H, for two reaction sequences: $Fe(OH)_2 + H$ followed by $FeOH + H$, comparing experiment (■) with model (−·−); and $FeO_3 + H$ followed by $FeOH + H$, comparing experiment (●) with model (—).

Using this value for k_7 in the model, we now optimise the fit to the second set of data points in Fig. 9a for the sequence $FeO_3 \rightarrow FeOH \rightarrow Fe$. This procedure yields $k_5 = (2.0^{+1.2}_{-0.6}) \times 10^{-11}$ cm^3 molecule^{-1} s^{-1}. Fig. 9b shows the χ^2
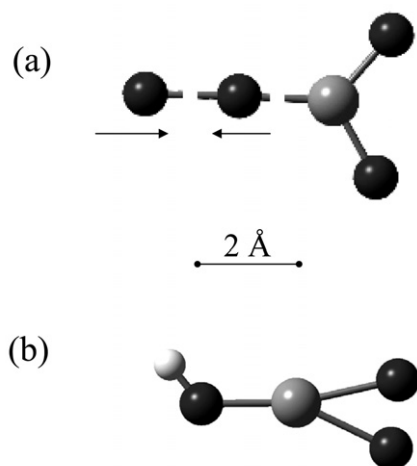

Fig. 10 (a) Transition state for the reaction $FeO_3 + O$ on the lowest-lying quintet surface and (b) quartet FeO_3H, calculated at the B3LYP/6-311+g (2d,p) level of theory.

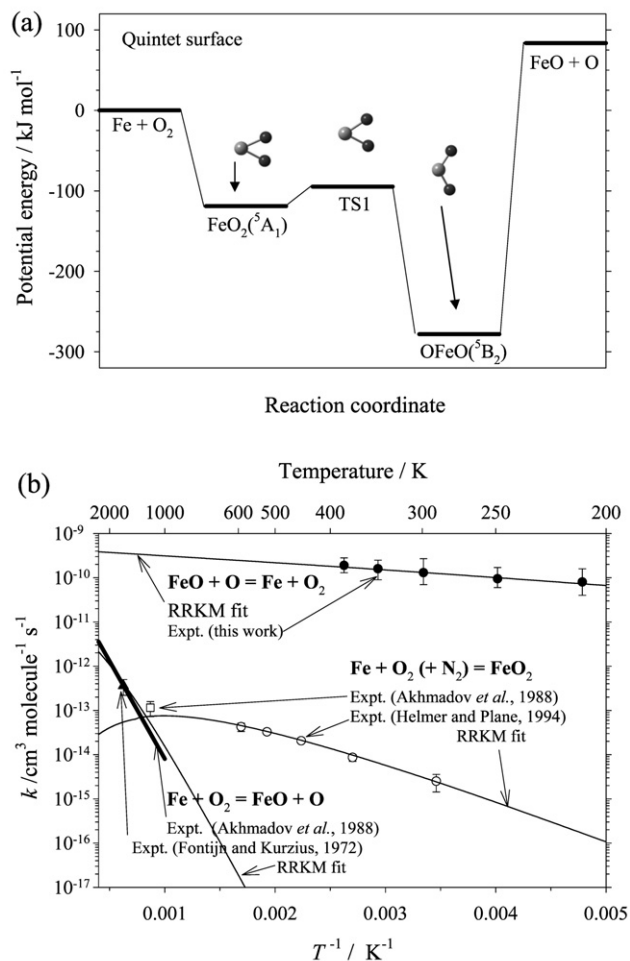**Fig. 11** (a) Lowest energy (quintet) potential energy curve for the $Fe + O_2 \leftrightarrow FeO + O$ system, calculated at the B3LYP/6-311+G(2d,p) level of theory. (b) RRKM calculated rate coefficients (thin solid lines) at a pressure of 20 Torr over the temperature range of 200–2000 K, for the following reactions: $FeO + O \rightarrow Fe + O_2$ (compared with the results of the present study); $Fe + O_2 (+N_2) \rightarrow FeO_2$ (compared with measurements by Helmer and Plane[4] and Akhmadov *et al.*[10]); and $Fe + O_2 \rightarrow FeO + O$ (compared with measurements by Fontijn and Kurzius[9] and Akhmadov *et al.*[10]).

surface evaluated using equation (III) as a function of k_5 and k_7. The arrows indicate the best fit value and the upper and lower limits of k_5, derived from the various experimental uncertainties and the uncertainty in k_7 derived above. Note that this χ^2 surface does not have a clear minimum (*cf.* Fig. 6b), demonstrating that k_5 and k_7 cannot both be derived from this data set alone.

Finally, an approximate estimate of the rate coefficient for the exothermic reaction

$$FeO_3 + H_2O \rightarrow Fe(OH)_2 + O_2 \quad \Delta H_0^\circ = -174 \text{ kJ mol}^{-1} \text{ }^5$$
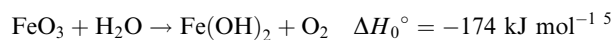
was determined by forming FeO_3 in the upstream section of the tube, and adding varying amounts of H_2O (up to 1.8×10^{14} cm^{-3}) further downstream through the sliding injector. A large concentration of H was then injected into the flow immediately before the spectroscopic cell, and %Fe measured as before. Because k_6 is larger than k_5, a small increase in %Fe was observed at high $[H_2O]$ as more FeO_3 was converted to $Fe(OH)_2$. However, reaction (7) is still the rate determining step in producing Fe, whether from FeO_3 or $Fe(OH)_2$, and so the observed increase in %Fe was not significant enough other than to yield a tentative rate coefficient, $k(FeO_3 + H_2O) \approx 5 \times 10^{-12}$ cm^3 molecule^{-1} s^{-1}, with an uncertainty factor of 2.5.

Discussion

In order to interpret the experimental results, a set of quantum calculations was performed on the relevant iron-containing species involved in reactions (1)–(7). The hybrid density functional/Hartree–Fock B3LYP method was employed from within the Gaussian 98 suite of programs,[31] together with the 6-311+G(2d,p) basis set. This is a high quality triple zeta basis set with both polarization and diffuse functions added to the atoms. At this level of theory, the expected uncertainty in the calculated reaction enthalpies is 13 kJ mol^{-1}.[32] The B3LYP/6-311+g(2d,p) method is well suited for calculations on transition metal compounds, as we have shown previously in the case of FeO, FeO$_2$ and FeOH, for which there are some experimental vibrational frequencies, rotational constants and dipole moments for comparison.[5,20]

Molecular geometries at the stationary points (minima and saddle points) on the potential energy surfaces were first optimised. For many of these molecules, the initial self consistent field (SCF) wavefunction was unstable and had to be re-optimised. The geometry optimisation was then completed and the respective vibrational frequencies calculated. The resulting dipole moments, rotational constants, vibrational frequencies and heats of formation are listed in Table 4. See Plane and Rollason[20] for the analogous data on OFeO and FeO$_2$, and Rollason and Plane[5] for calculations on FeO, OFeO$_2$, FeO$_3$ and FeOH.

We now consider the potential energy surfaces of reactions (3) and (5) in order to explain the difference in reactivity of O and H towards FeO$_3$. In our previous theoretical study of FeO$_3$,[5] we established that the two most stable forms are a singlet and a triplet, both with D_{3h} symmetry. Since in the present study FeO$_3$ was made from the reaction FeO($^5\Delta$) + O$_2$($^3\Sigma_g^-$), spin considerations suggest that triplet FeO$_3$ would have been formed in the flow tube, at least initially. Thus, reaction (3) involving O(^{3}P$_J$) could occur on singlet, triplet or quintet surfaces. Fig. 10a illustrates the geometry of the transition state on the (lowest-lying) quintet surface. Applying transition state theory using the molecular parameters listed in Table 4 and in ref. 2, we obtain the very satisfactory fit to the experimental data-points for reaction (3) in the Arrhenius plot illustrated in Fig. 7. This fit is achieved if the barrier height (with respect to the reactants) is set to 18.7 kJ mol^{-1}, which compares very well with the theoretical estimate of 21.8 kJ mol^{-1}. Of course, this agreement may be somewhat fortuitous considering the complexity of surfaces involved. The best fit of TST to the experimental data yields k_3(150–700 K) = $3.5 \times 10^{-10} \exp(-2386/T)$ cm^3 molecule^{-1} s^{-1}. Extrapolation to mesospheric temperatures is discussed below.

In the case of reaction (5), there is a very deep minimum on the PES corresponding to FeO$_3$H (illustrated in Fig. 10b), which is bound by 394 kJ mol^{-1} with respect to FeO$_3$ + H. However, FeO$_3$H is very unlikely to form in reaction (5) through recombination (at any reasonable third body
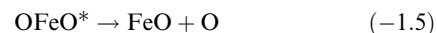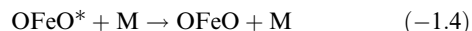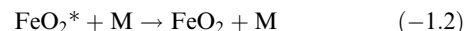
pressure) because the exit channel to FeOH + O$_2$ is exothermic by 221 kJ mol^{-1}. There is also no appreciable barrier in the entrance channel of the lowest-lying quartet surface, which explains why reaction (5) is relatively fast.

We now consider reaction (1). Both channels of the reverse reaction

$$\text{Fe} + \text{O}_2 \rightarrow \text{FeO}_2 \text{ or OFeO}(+\text{M}) \qquad (-1a)$$

$$\rightarrow \text{FeO} + \text{O} \qquad (-1b)$$

have been studied experimentally.[9,10,21] This system presents the opportunity to see if there is a consistent kinetic model that accounts for the experimental measurements on reactions (1), (−1a) and (−1b), over a large range of temperature. Fig. 11a illustrates the stationary points on the lowest-lying potential energy surface (PES) for reaction (1), which has quintet spin multiplicity. There are two minima, corresponding to the FeO$_2$(^{5}A$_1$) superoxide that forms initially when Fe and O$_2$ recombine;[21] and the more stable OFeO(^{5}B$_1$) dioxide, that is likely to form initially when O adds to FeO. These forms are connected through a saddle point (see Table 4 for details). Fig. 11a shows that this saddle point is well below the asymptotic energies of either Fe + O$_2$ or FeO + O, and should therefore not play a significant role in either reaction (1) or (−1).

RRKM theory was then applied to this system, using the Master Equation (ME) formalism described by De Avillez Pereira et al.[33] This formalism determines the microcanonical rate coefficients for dissociation of an adduct by using inverse Laplace transformation of the recombination rate coefficient at the high pressure limit. The application of this formalism to model reactions involving metallic species has been described by us in detail previously.[5] In the case of the Fe + O$_2$ ↔ FeO + O system, the following reactions were included:

$$\text{Fe} + \text{O}_2 \rightarrow \text{FeO}_2^* \qquad (-1.1)$$

$$\text{FeO}_2^* \rightarrow \text{Fe} + \text{O}_2 \qquad (1.1)$$

$$\text{FeO}_2^* + \text{M} \rightarrow \text{FeO}_2 + \text{M} \qquad (-1.2)$$

$$\text{FeO}_2^* \leftrightarrow \text{OFeO}^* \qquad (-1.3)$$

$$\text{OFeO}^* + \text{M} \rightarrow \text{OFeO} + \text{M} \qquad (-1.4)$$

$$\text{OFeO}^* \rightarrow \text{FeO} + \text{O} \qquad (-1.5)$$

The program was also extended using the approach of Hahn et al.[34] to describe the situation of a double well on the PES, illustrated in Fig. 11a. As shown in Fig. 11b, the experimental measurements on reactions (1), (−1a) and (−1b), which cover a wide range of temperature from 200–2000 K, can be very satisfactorily modelled using the following values for the adjustable parameters: the enthalpy change for reaction (1), $\Delta H_0(1)$, fitted to −84 kJ mol^{-1}; the average energy removed when FeO$_2^*$ or OFeO* collides with N$_2$, $\langle \Delta E \rangle_{\text{down}}$, set to 270 cm^{-1} at 300 K which is typical for this third body,[35] the

Table 4 Quantum calculations as the B3LYP/6-311+g(2d,p) level for selected stationary points on the potential energy surfaces for the reactions FeO + O, FeO$_2$ + O, FeO$_3$ + O, FeO$_3$ + H and FeOH + H

Species	Dipole moment[a]	Rotational constants[b]	Vibrational frequencies[c]	$\Delta H_{\text{f,0}}^{\circ d}$
OFeO# TS1 on quintet surface, Fig. 10	6.1	19.4, 11.4, 7.2	585i, 564, 796	310
OFeO$_2$# TS2 on triplet surface, Fig. 11	2.4	14.0, 5.34, 4.25	509i, 178, 220, 534, 752, 1033	237
O–OFeO$_2$# Quintet, Fig. 10a	2.0	8.89, 2.17, 1.75	723i, 56, 80, 276, 326, 419, 453, 850, 901	373
FeO$_3$H Quartet, Fig. 10b	2.0	33.6, 3.14, 2.87	99, 125, 211, 282, 447, 550, 716, 1167, 3894	−66
FeO–H$_2$# TS3 on quintet surface, Fig. 13	5.2	103, 13.6, 12.0	1240i 642, 829, 983, 1639, 1980	272
Fe–OH$_2$# TS4 on quintet surface, Fig. 13	1.3	244, 10.0, 9.86	1228i, 443, 523, 767, 1385, 3772	236

[a] In Debye (= 3.336×10^{-30} C m). [b] In GHz. [c] In cm^{-1}. [d] In kJ mol^{-1}, uncertainty ± 20 kJ mol^{-1}. Calculated with respect to $\Delta H_{\text{f,0}}^0$ for FeO, FeO$_2$, FeO$_3$ and FeOH in refs. 3 and 4.

rate constant for collision between FeO_2^* or $OFeO^*$ and N_2, fitted to 5.7×10^{-10} cm^3 molecule^{-1} s^{-1} at 300 K; and the recombination rate coefficient at the high pressure limit for $Fe + O_2$, $k_{rec,\infty}$, fitted to 6.2×10^{-10} exp$(-433/T)$ cm^3 molecule^{-1} s^{-1}.

As stated above, the objective in carrying out the RRKM modelling was to confirm that the diverse experimental measurements on reactions (1), (−1a) and (−1b) could be explained by a single model. However, because none of these reactions was studied over the entire temperature range by a single technique, a detailed sensitivity analysis on the fitted parameters is of limited value. Nevertheless, the ratio of k_1 to k_{-1b} as a function of T is a sensitive test of the fitted value of $\Delta H_0(1)$ in the RRKM model. Although these rate coefficients were measured over different temperature ranges (209–381 K and 1000–2500 K, respectively), satisfactory fits (i.e., within the experimental uncertainties) can only be obtained if $\Delta H_0(1)$ lies between −81 and −89 kJ mol^{-1}. This range compares well with the experimental estimate of −91 ± 8 kJ mol^{-1} based on $D_0(Fe–O) = 402 \pm 8$ kJ mol^{-1},[5] and is in reasonable accord with our theoretical estimate of −74 ± 13 kJ mol^{-1} based on $D_0(Fe–O) = 419 \pm 13$ kJ mol^{-1}.[5]

In the case of reaction (2), there are also two channels for the reverse reaction:

$$FeO + O_2 \rightarrow FeO_3 \text{ or } OFeO_2 \quad (+M) \qquad (-2a)$$

$$\rightarrow FeO_2 + O \qquad (-2b)$$

Fig. 12a shows that the lowest-lying (triplet) potential energy curve also has two minima corresponding to $OFeO_2$ and FeO_3. However, in contrast to reaction (1), the barrier between these forms lies only slightly below the asymptotic energy limit of $FeO + O_2$ and therefore has more influence on the kinetics of reaction (−2). Fig. 12b shows that a very good fit of RRKM theory is achieved to the experimental measurements on $FeO_2 + O$ from the present work and a high temperature flame study,[12] as well as the recombination of FeO and O_2 from our previous study.[5] Note that the individual recombination reactions to form FeO_3 and $OFeO_2$ make similar contributions to the total k_{-2a}, in spite of $OFeO_2$ being significantly less strongly bound. There are two reasons for these similar contributions: the role of the barrier (TS2) preventing ready access to the deeper well of FeO_3; and the very low vibrational frequencies of $OFeO_2$ (122 and 133 cm^{-1} [5]) which indicate that this molecule should be treated as a 2-dimensional free internal rotor $(FeO–O_2)$.[5]

Fig. 12b also shows that reaction (−2b) should be very slow even up to flame temperatures. The following parameters were used to fit to the experimental data: the enthalpy change for reaction (2), $\Delta H_0(2) = -107.0$ kJ mol^{-1}, compared with −118 ± 46 kJ mol^{-1} based on $D_0(Fe–O_2) = 284 \pm 38$ kJ mol^{-1};[20] the average energy removed when FeO_3^* or $OFeO_2^*$ collide with N_2, $\langle \Delta E \rangle_{down} = 270$ cm^{-1}; the rate constant for collision between FeO_3^* or $OFeO_2^*$ and N_2, fitted to 5.5×10^{-10} cm^3 molecule^{-1} s^{-1} at 300 K; the recombination rate coefficient at the high pressure limit for $FeO + O_2$, $k_{rec,\infty} = 1.4 \times 10^{-10}$ exp$(-582/T)$ cm^3 molecule^{-1} s^{-1}.

Fig. 13a illustrates the PES for reaction (7), which has three exothermic channels:

$$FeOH + H \rightarrow Fe + H_2O \qquad (7a)$$

$$\rightarrow FeO + H_2 \qquad (7b)$$

$$\rightarrow HFeOH(+M) \qquad (7c)$$
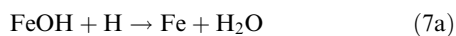
The features of this surface are in very good agreement with two other *ab initio* quantum studies that have been published recently.[36,37] Note that reaction (7a) has both a lower saddle point (TS4) and is more exothermic than reaction (7b), and so the RRKM theory predicts that reaction (7a) should be
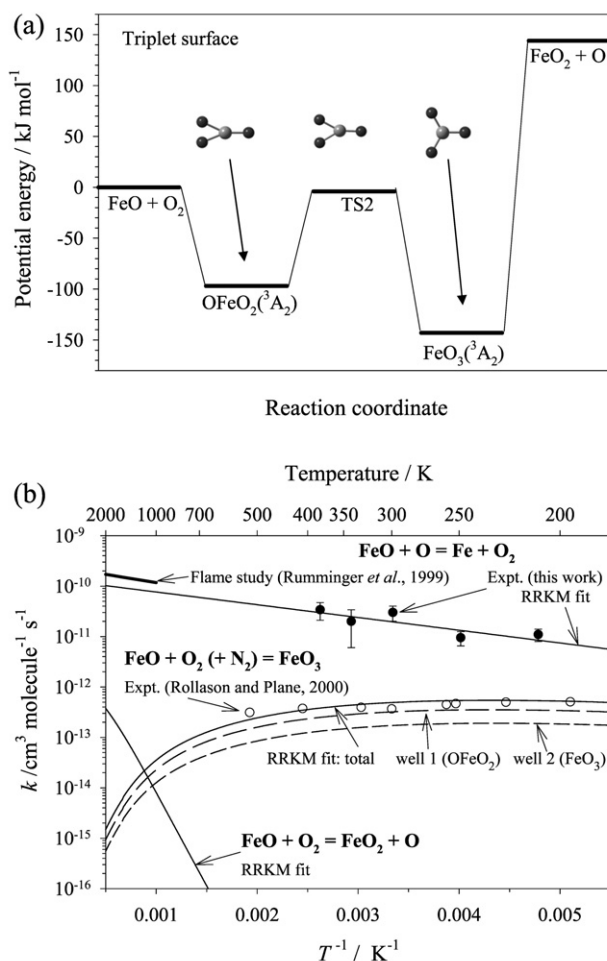
Fig. 12 (a) Lowest energy (triplet) potential energy curve for the $FeO + O_2 \leftrightarrow FeO_2 + O$ system, calculated at the B3LYP/6-311+G(2d,p) level of theory. (b) RRKM calculated rate coefficients (thin solid lines) at a pressure of 3.4 Torr over the temperature range of 200–2000 K, for the following reactions: $FeO_2 + O \rightarrow FeO + O_2$ (compared with measurements from the present study and by Rumminger *et al.*[12]); $FeO + O_2 (+N_2) \rightarrow FeO_3$ (compared with measurements by Rollason and Plane[5]); and $FeO + O_2 \rightarrow FeO_2 + O$.

the dominant channel. The following parameters were used to fit reaction (7a) to our experimental data point at 294 K: the average energy removed when HFeOH collides with N_2, $\langle \Delta E \rangle_{down} = 270$ cm^{-1}; the rate constant for collision between HFeOH* and N_2, set to 5.5×10^{-10} cm^3 molecule^{-1} s^{-1} at 300 K; the recombination rate coefficient at the high pressure limit for FeOH + H, $k_{rec,\infty} = 2.5 \times 10^{-10}$ exp$(-805/T)$ cm^3 molecule^{-1} s^{-1}.

The results of RRKM calculations on reaction (7), at a pressure of 1 atm to compare with the flame study, are illustrated in Fig. 13b. The figure shows that k_{7a} should be about an order of magnitude higher than k_{7b}, over the entire temperature range from 200 to 2000 K. Furthermore, even though the HFeOH minimum is 301 kJ mol^{-1} below the reactants, the saddle points TS3 and TS4 are sufficiently far below the energy of the reactants FeOH + H (56 and 92 kJ mol^{-1}, respectively), that formation of HFeOH should be negligible, except at temperatures well below 200 K.

Comparing the RRKM prediction with the flame study of Rumminger *et al.*[12] reveals a serious discrepancy, since those authors deduced that reaction (7b) is the dominant channel (Fig. 13b). Their conclusion was based on modelling the observed reduction of the burning velocity of a flame into which iron had been seeded. Their reaction scheme required the iron to cycle sufficiently rapidly between $Fe(OH)_2$ and
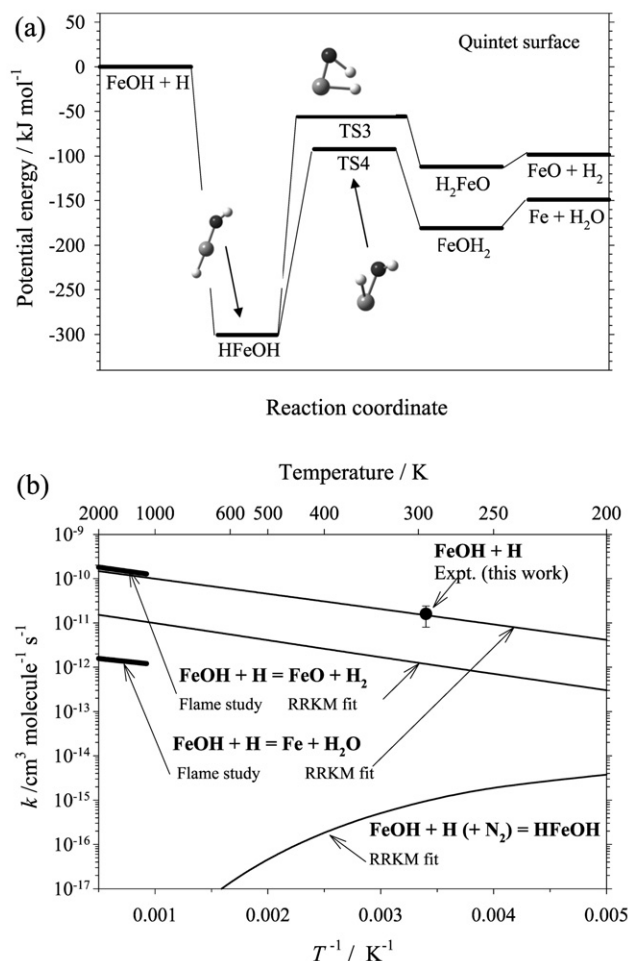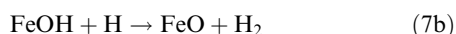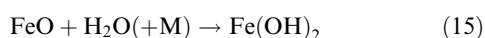
(a)

(b)

Fig. 13 (a) Potential energy curves (quintet multiplicity) for the reaction between FeOH and H producing either $FeO + H_2$ or $Fe + H_2O$, calculated at the B3LYP/6-311+G(2d,p) level of theory. (b) RRKM calculated rate coefficients (thin solid lines) at a pressure of 760 Torr over the temperature range of 200–2000 K, for the following reactions: $FeOH + H \rightarrow Fe + H_2O$ or $FeO + H_2$ (compared with the measured k_7 from the present study, and individual rate coefficients from Rumminger *et al.*[12]); and $FeOH + H (+N_2) \rightarrow HFeOH$.

FeO to catalyse the recombination of H:

$$FeO + H_2O(+M) \rightarrow Fe(OH)_2 \tag{15}$$

$$Fe(OH)_2 + H \rightarrow FeOH + H \tag{6}$$

$$FeOH + H \rightarrow FeO + H_2 \tag{7b}$$

$$\text{Net}: H + H \rightarrow H_2$$

Therefore, if reaction (7a) is the major pathway, then Fe must be re-oxidised to FeO more efficiently in flames than currently understood, or else other catalytic cycles may be involved.

Another point to note is that in the present study of reaction (7), Fe production was actually observed. Thus, if reaction (7) is the dominant channel, then the reaction $FeO + H \rightarrow Fe + OH$ ($\Delta H_0 = -26 \pm 8$ kJ mol^{-1})[5] is required by the flow tube model to proceed at $\approx 2.4 \times 10^{-10}$ cm^3 molecule^{-1} s^{-1} at 294 K (in order to compete with $FeO + O_2$ or H_2O). By contrast, the flame model[12] estimate of $k(FeO + H) = 1.7 \times 10^{-10}$ e$^{-3020/T}$ cm^3 molecule^{-1} s^{-1} extrapolates to 6×10^{-15} cm^3 molecule^{-1} s^{-1} at 294 K. It is clear that further work is required to resolve these discrepancies. In particular, if a suitable spectroscopic probe for FeOH could be found, then the pathways of reaction (7) could be studied directly.

Implications for the chemistry of iron in the upper mesosphere

The study reported here has elicited kinetic information about a number of reactions of iron-containing species with O and H. As a first step to determining which of the species illustrated in Fig. 1 is an important reservoir species in the upper mesosphere, we now consider the e-folding (or reaction) time constants of these reactions. The reaction time constant is the inverse of the product of the rate coefficient and the concentration of O or H, taken from an atmospheric model. It reflects the time taken for the reaction to proceed approximately 65% $(1 - e^{-1})$ towards completion, and thus provides a sensible measure of the lifetime of the iron species involved.

Fig. 14 illustrates atmospheric height profiles of the e-folding time constants for the reactions of the iron oxides and hydroxides with O and H. The conditions are January, 40°N at midnight.[6] In order to extrapolate to mesospheric temperatures (140–240 K), the temperature dependences for k_1 and k_2 measured in the present study were used. For reaction (5), an assumed Arrhenius pre-exponential factor of 3×10^{-10} cm^3 molecule^1 s^{-1} was combined with k_5(294 K) to yield an activation energy of 796 K. For reactions (6) and (7), the Arrhenius expressions derived from the flame study,[12] which are consistent with the present study at 294 K, were employed.

Fig. 14 shows that FeO and FeO_2 are very short-lived above 80 km, with lifetimes of less than 20 s. The reaction between $Fe(OH)_2$ and H ensures that the di-hydroxide has a lifetime of less than *ca.* 20 min. FeO_3 and FeOH are clearly the important reservoir species, at least within our current understanding of the mesospheric chemistry of iron (Fig. 1). Nevertheless, at altitudes between 80 and 95 km, where neutral chemistry controls the Fe layer, the lifetimes of these two species are less than 2 h. Rapid chemistry is essential in order to maintain the sharp underside of the Fe layer (see Introduction), since the chemical turnover time must be short compared with vertical eddy transport.[2] Interested readers are referred to a paper describing the incorporation of the results of the present study into a new mesospheric model of iron.[38]

Finally, we note that FeOH is most likely the dominant reservoir for atomic Fe below 95 km, because of the observation in the present study that FeO_3 reacts reasonably rapidly with H_2O to form $Fe(OH)_2$, which will then react with H to produce FeOH. Future work should therefore focus on FeOH—its photochemistry, and possible reactions with O_3 and O to form Fe(O)OH, a probable component of meteoric smoke particles.[8]
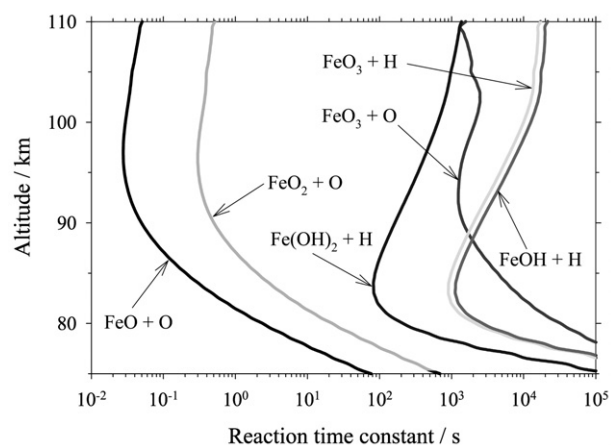

Fig. 14 Height profiles in the upper mesosphere/lower thermosphere of the e-folding time constants for a series of reactions involving iron oxides and hydroxides with O and H. Conditions: January, 40°N, midnight.

References

1 J. M. C. Plane, *Int. Rev. Phys. Chem.*, 1991, **10**, 55.
2 J. M. C. Plane, R. M. Cox and R. J. Rollason, *Adv. Space Res.*, 1999, **24**, 1559.
3 X. Z. Chu, W. L. Pan, G. C. Papen, C. S. Gardner and J. A. Gelbwachs, *Appl. Opt.*, 2002, **41**, 4400.
4 M. Helmer and J. M. C. Plane, *J. Chem. Soc., Faraday Trans.*, 1994, **90**, 31.
5 R. J. Rollason and J. M. C. Plane, *Phys. Chem. Chem. Phys.*, 2000, **2**, 2335.
6 M. Helmer, J. M. C. Plane, J. Qian and C. S. Gardner, *J. Geophys. Res. [Atmos.]*, 1998, **103**, 10 913.
7 D. M. Hunten, R. P. Turco and O. B. Toon, *J. Atmos. Sci.*, 1980, **37**, 1342.
8 F. J. M. Rietmeijer, *Planet. Space Sci.*, 2001, **49**, 71.
9 A. Fontijn and S. C. Kurzius, *Chem. Phys. Lett.*, 1972, **13**, 507.
10 U. S. Akhmadov, I. S. Zaslonko and V. N. Smirnov, *Kinet. Catal.*, 1988, **29**, 251.
11 D. E. Jensen and G. A. Jones, *J. Chem. Phys.*, 1974, **60**, 3421.
12 M. D. Rumminger, D. Reinelt, V. Babushok and G. T. Linteris, *Combust. Flame*, 1999, **116**, 207.
13 F. Kaufman, *Proc. R. Soc.London, Ser. A*, 1958, **247**, 123.
14 R. M. Cox, D. E. Self and J. M. C. Plane, *J. Geophys. Res.*, 2001, **106**, 1733.
15 R. W. Huggins and J. H. Kahn, *J. Appl. Phys.*, 1967, **38**, 180.
16 M. Helmer and J. M. C. Plane, *J. Geophys. Res.*, 1993, **98**, 23 207.
17 *Handbook of Physics and Chemistry*, ed. D. R. Lide, CRC Press, Boca Raton, FL, 78th. edn., 1997.
18 A. A. Radzig and B. M. Smirnov, *Reference Data on Atoms, Molecules and Ions*, Springer-Verlag, Berlin, 1985; J. R. Fuhr and G. A. Martin, W. L. Wiese, S. M. Younger, *J. Phys. Chem. Ref. Data*, 1981, **10**, 305.
19 S. A. Mitchell and P. A. Hackett, *J. Chem. Phys.*, 1990, **93**, 7813.
20 J. M. C. Plane and R. J. Rollason, *Phys. Chem. Chem. Phys.*, 1999, **1**, 1843.
21 M. Helmer and J. M. C. Plane, *J. Chem. Soc., Faraday Trans.*, 1994, **90**, 395.
22 S. A. Mitchell and P. A. Hackett, *J. Chem. Phys.*, 1990, **93**, 7822.
23 R. Atkinson, D. L. Baulch, R. A. Cox, R. F. Hampson, Jr., J. A. Kerr, M. J. Rossi and J. Troe, *J. Phys. Chem. Ref. Data*, 1997, **26**, 1329.
24 G. C. Maitland, M. Rigby, E. Brian Smith and W. A. Wakeham, *Intermolecular Forces: Their Origin and Determination*, Oxford University Press, Oxford, 1987.
25 W. H. Press, B. P. Flannery, S. A. Teukolsky and W. T. Vetterling, *Numerical Recipes*, Cambridge University Press, 1987.
26 D. E. Self and J. M. C. Plane, *Phys. Chem. Chem. Phys.*, 2002, **4**, 16.
27 B. J. Murray and J. M. C. Plane, *School of Environmental Sciences*, University of East Anglia (j.plane@uea.ac.uk).
28 S. G. Lias, J. E. Bartmess, J. F. Liebman, J. L. Holmes, R. D. Levin, and W. G. Mallard, Gas-phase ion and neutral thermochemistry, *J. Phys. Chem. Ref. Data*, 1988, 17.
29 J. M. C. Plane and R. J. Rollason, *J. Chem. Soc., Faraday Trans.*, 1996, **92**, 4371.
30 J. R. Taylor, *An Introduction to Error Analysis: The Study of Uncertainties in Physical Measurements*, ch.8, Oxford University Press, Oxford, 1982.
31 M. J. Frisch, G. W. Trucks, H. B. Schlegel, G. E. Scuseria, M. A. Robb, J. R. Cheeseman, V. G. Zakrzewski, J. A. Montgomery, Jr., R. E. Stratmann, J. C. Burant, S. Dapprich, J. M. Millam, A. D. Daniels, K. N. Kudin, M. C. Strain, O. Farkas, J. Tomasi, V. Barone, M. Cossi, R. Cammi, B. Mennucci, C. Pomelli, C. Adamo, S. Clifford, J. Ochterski, G. A. Petersson, P. Y. Ayala, Q. Cui, K. Morokuma, D. K. Malick, A. D. Rabuck, K. Raghavachari, J. B. Foresman, J. Cioslowski, J. V. Ortiz, B. B. Stefanov, G. Liu, A. Liashenko, P. Piskorz, I. Komaromi, R. Gomperts, R. L. Martin, D. J. Fox, T. Keith, M. A. Al-Laham, C. Y. Peng, A. Nanayakkara, C. Gonzalez, M. Challacombe, P. M. W. Gill, B. G. Johnson, W. Chen, M. W. Wong, J. L. Andres, M. Head-Gordon, E. S. Replogle and J. A. Pople, *GAUSSIAN 98 (Revision A.7)*, Gaussian, Inc., Pittsburgh, PA, 1998.
32 J. B. Foresman and A. Frisch, *Exploring chemistry with electronic structure methods*, Gaussian, Inc., Pittsburgh PA, 1996.
33 R. De Avillez Pereira, D. L. Baulch, M. J. Pilling, S. H. Robertson and G. Zeng, *J. Phys. Chem. A*, 1997, **101**, 9681.
34 D. K. Hahn, S. J. Klippenstein and J. A. Miller, *Faraday Discuss.*, 2001, **119**, 79.
35 R. G. Gilbert, S. C. Smith, *Theory of Unimolecular and Recombination Reactions*, Blackwell, Oxford, 1990.
36 L. M. Zhang, L. Zhou, W. Shao, K. Wang, K. Fan and Q. Qin, *J. Phys. Chem. A*, 2001, **105**, 6998.
37 A. M. Mebel and D-Y. Hwang, *J. Phys. Chem. A*, 2001, **105**, 7460.
38 J. M. C. Plane, D. E. Self, T. Vondrak and K. R. Woodcock, *Adv. Space Res.*, in press.